

1. Assessment of the Sub-Daily Global Satellite Precipitation Products

1.1. Intrinsic uncertainty in the sub-daily satellite products at their native resolutions

Ziad S. Haddad¹, Francis J. Turk¹, Nobuyuki Utsumi² and Pierre-Emmanuel Kirstetter³

¹Jet Propulsion Laboratory, California Institute of Technology, Pasadena, CA, USA

²Nagamori Institute of Actuators, Kyoto University of Advanced Science, Kyoto, Japan

³University of Oklahoma, Norman, OK, USA

1.1.1. Background

For many hydrological and weather forecasting applications, an important quantity is the amount of precipitation that falls on the Earth's surface over a given time interval, i.e., the surface precipitation rate. However, no satellite instrument is unambiguously sensitive to the instantaneous precipitation rate at the Earth's surface. A vertically profiling radar such as the Dual-Frequency Precipitation Radar (DPR) onboard the joint National Aeronautics and Space Administration (NASA) and Japanese Aerospace Exploration Agency (JAXA) Global Precipitation Measurement (GPM) mission satellite (Hou et al., 2014) is directly sensitive to rain in the near-surface layers of the atmosphere unaffected by surface ground clutter, but its measurements are affected by attenuation due to the condensed water in the higher layers of the cloud. Furthermore, the DPR instrument scan swath is typically too narrow (240 km) to provide substantial global coverage at sub-weekly scales. Passive microwave (MW) radiometers do have more substantial coverage owing to their wider swath (between 800 and 2500 km). These measurements are less directly sensitive to surface rain, with more direct sensitivity to the condensed water in the cloud. The height of the "peak" sensitivity increases as the radiometer channel wavelength decreases, up to infrared (IR) radiometers, which are directly sensitive only to the condensed water at the very top of the cloud (Haddad et al., 2017). IR radiometers are now carried by all meteorological geostationary satellites, providing global coverage with very frequent temporal sampling (at least every 30 minutes or better).

Therefore, the algorithms that generate today's global satellite precipitation products attempt to capitalize on the different strengths of these three types of instrument (radar, passive MW radiometers and frequent-refresh IR radiometers). These algorithms rely upon the reasonable sensitivity of the microwave radiometers, sharpened by reference to the precipitation radars, and enlist the help of IR to interpolate the microwave estimates to the often-long intervals of time between consecutive passive MW observations. These "revisit gaps" can be 5 hours in the tropical latitudes (Kidd et al., 2018a). As a result, one expects three broad sources of uncertainty in the products: a detection-related uncertainty that results from the possible confusion in the interpretation of the passive MW or IR observations between surface rain and cloud-column condensation; an estimation uncertainty that results from the quantitative conversion of the passive MW or IR observations into surface-rain amounts; and an interpolation issue stemming from the ambiguous use of frequent-but-indirectly-sensitive IR information to fill the revisit gaps.

To illustrate this general approach, Figure 1.1.1 depicts an *idealized* set of observations collected from four passive MW satellite overpasses over a given location during a 12-hour period. The data from each passive MW satellite measurement provide an estimate of the

surface precipitation (blue arrows). In this example, the satellites are equally spaced in their observing times, leaving 3-hour revisit gaps. By combining and merging these data with higher time resolution geostationary satellite data, the desired high spatial and temporal resolution precipitation products are produced (denoted by the red arrows). The errors resulting from the combination of all of the processing steps mentioned above are aggregated into the final high-resolution products that are provided to data users. Most often, the error analysis is carried out on the products that are produced at the end of this process, which represents an accumulated error. The purpose of this section is to provide insight to product users on the nature of the error introduced by the various steps. The remainder of this section is devoted to the discussion of these error components in more detail.

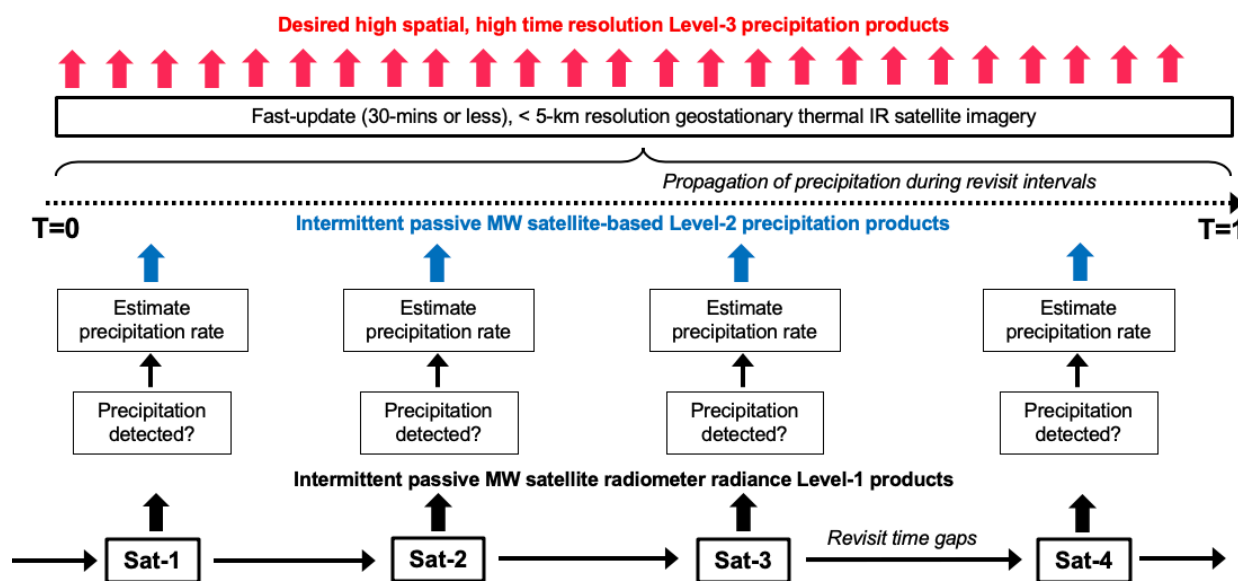


Figure 1.1.1. Idealized depiction showing how intermittent passive MW satellite-based precipitation data (blue arrows) are generated from a limited set of satellite overpasses, and used to produce a high spatial and temporal resolution (red arrows) satellite precipitation product

1.1.2. Satellite precipitation measurements

For the past two decades, the centerpieces of satellite precipitation measurements from space are the GPM core spacecraft (2014–present) and its predecessor, the Tropical Rainfall Measuring Mission (TRMM) (1997–2014) (Kummerow et al., 2000). Only these two spacecraft have a scanning precipitation radar instrument. TRMM and GPM’s passive MW radiometers observe precipitation across scan swaths that are much wider (800 km) than the respective radar swath, and indeed the radar measurements are used as benchmarks, available over the common narrow swath, to guide the estimation of surface rain from the passive MW radiometers alone outside the common swath. Yet the swath of each passive MW radiometer is still not wide enough to allow global coverage on sub-daily time scales (i.e. revisit periods of less than 24 hours, let alone three or less as in the example of Figure 1.1.1). That is why the estimates at sub-daily scales require the aggregation of estimates from all available passive MW radiometers. Table 1 of Kidd et al. (2018a) lists the characteristics of the current GPM passive MW radiometers [GPM microwave imager (GMI), Special Sensor Microwave Imager/Sounder (SSMIS), Advanced Microwave Scanning Radiometer 2 (AMSR-2), Microwave Humidity Sounder (MHS) and Advanced Technology Microwave Sounder (ATMS)].

Many of these passive MW radiometers are carried by operational weather satellites, which orbit in sun-synchronous patterns and produce observations near fixed local solar times (so their observations can be efficiently assimilated into numerical weather prediction systems). Others, like GPM, TRMM and the Megha-Tropiques (M-T) satellite built by the Indian Space Research Organization (ISRO) and the French Centre National d'Etudes Spatiales (CNES), orbit in non-sun-synchronous orbits whose local observing times change from day to day, in 30–60-day cycles (depending upon latitude) (Roca et al., 2015; Negri et al., 2002). In contrast to the idealized depiction of Figure 1.1.1, Figure 1.1.2 shows a more realistic set of passive MW observations from the current (2020) GPM-era constellation, whose revisits, unlike Figure 1.1.1, are not evenly spaced in time. Moreover, these consist of different types of radiometers with different channels, resolutions and sensitivities. Therefore, the detection and estimation errors shown in Figure 1.1.1 are different for each sensor.

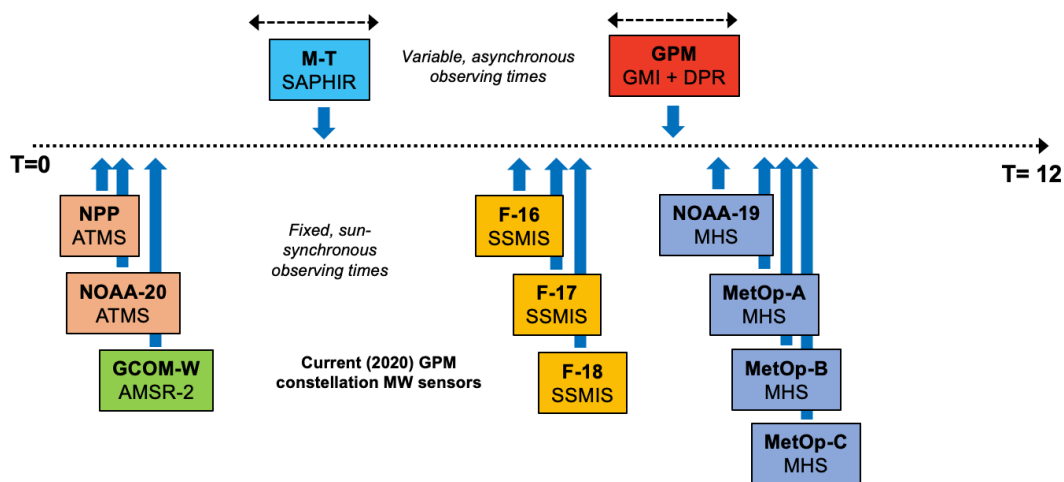


Figure 1.1.2. Depiction of the different passive MW satellites and their capabilities, observing times and revisit intervals during a typical 12-hour period, from the current (2020) GPM constellation era (contrast to idealized Figure 1.1.1)

The sensitivity of the passive MW radiometers is different for different radiometers and for different cloud types. These radiometers measure the net upwelling radiation from the Earth's surface through the atmosphere, in different frequency bands. The upwelling radiation comes primarily from the surface, and is modulated by the constituents of the atmosphere: the gases absorb (and therefore emit), and the hydrometeors (rain drops and the varieties of ice, snow, graupel, etc.) absorb/emit and also scatter the upwelling radiation, mostly out of the beam. This explains why the passive MW radiometers are not specifically sensitive to the precipitation in any single height layer of the cloud, let alone the surface layer. The radars, on the other hand, do not have this limitation, and do enable the estimation of vertical precipitation profiles. That is the justification for the multi-channel passive MW retrieval techniques which use a reference set of nearly-coincident nearly-simultaneous radar measurements (compiled offline, pairing passive MW measurements with the underlying precipitation rates as retrieved from the coincident simultaneous radar measurements), to produce instantaneous surface-rain estimates. These data can indeed be used to spread or "transfer" the DPR/Precipitation Radar (PR) radar structure information to each of the constellation radiometers (e.g., Turk et al., 2018; Kidd et al. 2018a; Petty and Li, 2013), so that each "Level-1" radiometer pixel can be assigned a "Level-2" estimate of the surface precipitation rate. The coincidence reference dataset can be used to retrieve any quantity that can be retrieved from the precipitation radar's measurements, with varying amounts of uncertainty that can be quantified from the reference data themselves, if the reference data are sufficiently extensive to be representative of global precipitation. Fortunately, both GPM and TRMM have asynchronous orbits so that, throughout the course of

a year, they do provide a very large number of near-coincident observations with each of the constellation radiometer satellites.

Lastly, the collection of Level-2 passive MW precipitation products is incorporated into global products covering a time interval, posted at a fixed grid resolution that can be near or finer than the scale of some of the Level-2 products that were used. These are termed “Level-3” products, which provide accumulated precipitation estimates at scales as fine as 30-minute refresh cycles, and 0.1° gridded resolution. For the remainder of this section, the focus is on the Level-3 products that incorporate the Level-2 passive MW precipitation products and high-resolution, fast-refresh cycle geostationary-satellite infrared (IR) observations to cover what would otherwise be lengthy revisit gaps from the Level-2 passive MW precipitation alone.

The next subsection attempts to quantify the order of magnitude of the uncertainties in the Level-3 products separately for each of the three sources of uncertainty. Examples of current widely-used global Level-3 precipitation products of this type include the Integrated Multi-Satellite Retrievals for GPM (IMERG) (Huffman et al., 2018); the Global Satellite Mapping of Precipitation (GSMaP) (Ushio et al., 2009), the National Oceanic and Atmospheric Administration (NOAA) Climate Prediction Center Morphing Technique (CMORPH) (Joyce and Xie, 2011), the Precipitation Estimation from Remotely Sensed Information using Artificial Neural Networks (PERSIANN) (Hsu et al., 1997), and the Self-Calibrating Multivariate Precipitation Retrieval (SCaMPR) (Kuligowski et al., 2013). A description and an intercomparison of many current global precipitation datasets from stations and satellites can be found in Sun et al. (2018). Because they are published at such relatively high spatial and temporal resolution, it is important to give an objective assessment of the uncertainty in these values at their reported resolution.

1.1.3. Intrinsic uncertainty of the Level-3 merged products

Early evaluation initiatives of a number of research Level-3 products were fostered by the International Precipitation Working Group (IPWG) (Ebert et al., 2007; Turk et al., 2008 and references within; see also 1.3 below). More recently in the post-GPM era, more detailed Level-3 evaluation efforts have been reported. A detailed list of these evaluation efforts would be lengthy (and likely incomplete); for reference, we refer to several recently-published studies (Maranan et al., 2020; Le Coz et al., 2020; Chen et al., 2019; Tan et al., 2016; Maggioni et al., 2014) and references within each of these. These studies generally proceed by comparing the values that are reported by a given product with other precipitation estimates. In contrast, in this subsection we review the uncertainties due to the sources of error in the successive steps in the estimation process. Indeed, the Level-3 uncertainty is the result of the accumulated uncertainty in the different steps of the estimation process, which for the purposes here are assumed to start with the Level-2 precipitation products themselves.

There are three main sources of uncertainty: 1) the uncertainty introduced in the precipitation detection by the Level-2 passive MW algorithms (either by omission, if no precipitation is detected so that the retrieval algorithm is not run and the precipitation is assumed to be zero when in fact precipitation was present, or by processing the passive measurements through the retrieval process when in reality there was no rain at the surface); 2) for the detected pixels, the uncertainty introduced by the instantaneous retrieval algorithms; and 3) the uncertainty introduced by the revisit-gap mitigation, i.e. the propagation in time from one Level-2 passive MW precipitation estimate to the next (i.e. from the Level-2 passive MW precipitation at time-1, to the passive MW precipitation at time-2).

In the following subsections, the Level-3 propagation-based methods common to operationally-produced precipitation products – IMERG, CMORPH, and GSMaP – are used as examples in the discussion of the third error component (use of IR data to fill passive MW revisit gaps). Products other than these three use different approaches to bring passive MW information to bear on IR data, including self-calibration (as in the case of SCaMPR) or artificial neural networks (as in the case of PERSIANN). The fundamental source of uncertainty in these mostly IR-based products is discussed in 1.1.3.5.

1.1.3.1. Detection errors

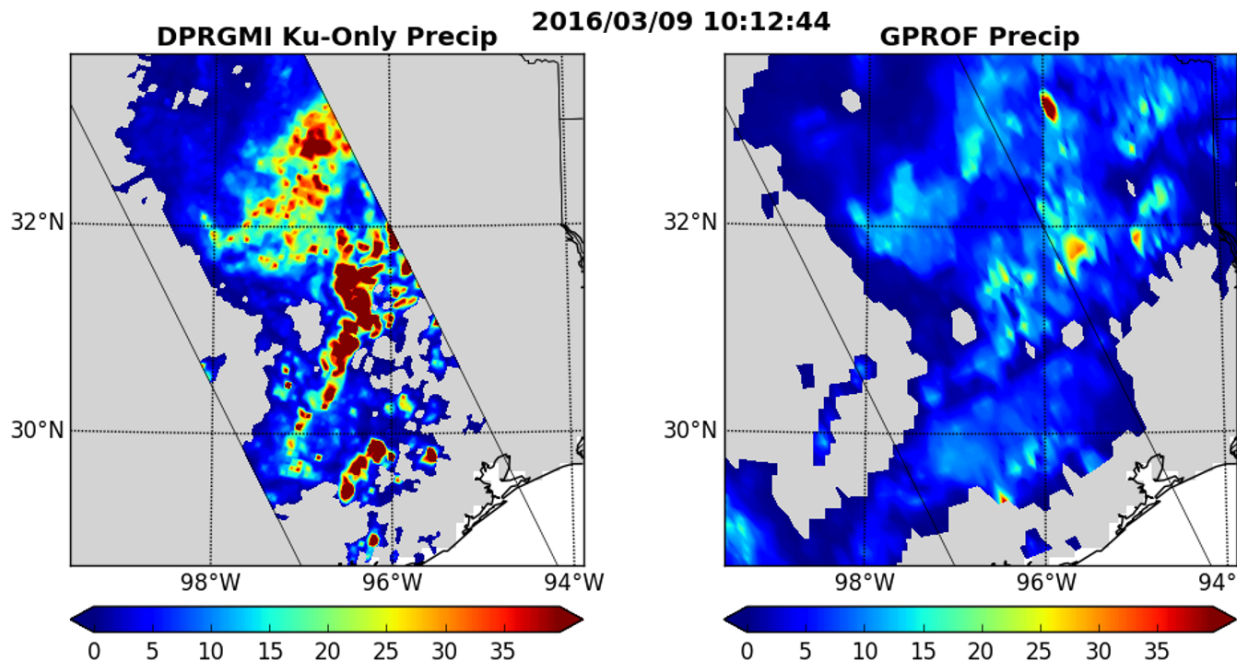


Figure 1.1.3. Side-by-side comparison of the precipitation estimate produced by the GPM combined DPR+GMI (CORRA) product (left panel), and the corresponding GMI-only (GPROF) estimate (right panel).

Establishing the minimum detectable precipitation rate for the Level-2 passive MW algorithms is not a straightforward proposition. The issue is illustrated in Figure 1.1.3, showing a typical pair of instantaneous retrievals, one made by the GMI radiometer algorithm (Goddard Profiling Algorithm, GPROF) (Kummerow et al., 2015) and one by the GPM combined sensor (DPR+GMI) radar radiometer algorithm (Combined Ku Radar-Radiometer Algorithm, CORRA) (Greco et al., 2016). The substantial areas where the GMI algorithm detects surface precipitation > 0 mm/hr while the CORRA algorithm reports 0 mm/hr surface rain could indicate a greater (if indirect) sensitivity of GMI to lower precipitation rates than the radar, or they could be false alarms where passive MW retrievals were made over a precipitation-free column. In these discrepancies, the radiometer-retrieved rates are never greater than a few mm/hr, yet they do cover a significant area. The reverse can happen too (in the case illustrated, most notably in the area around 29N 96.5W), though this “failure to detect” by the instantaneous passive MW radiometer retrieval algorithms is less common.

Using a research passive MW precipitation profiling method (emissivity principal components, EPC) (Turk et al., 2018) based on the microwave surface emissivity, Utsumi et al. (2020) showed that the probability of detection (POD) over ocean surfaces exceeded 0.7 and was fairly consistent across the five algorithms tested and the choice of precipitation threshold. Over land, POD can drop below 0.6 for vegetated surfaces or coasts (Turk et al., 2018). Similar POD

scores were noted across passive MW sensors (You et al., 2020). Chen et al. (2019) performed a similar experiment and concluded that the conically-scanning imagers generally outperformed the cross-track scanning sounders.

1.1.3.2. Errors inherent to the instantaneous passive MW retrievals

Compared to the Level-3 products, relatively few independent validation studies of Level-2 passive MW constellation products have been done. A comparison of the areas with larger surface rain rates in Figure 1.1.3 illustrates the intrinsic uncertainty in the Level-2 instantaneous retrievals from passive MW measurements. Note how the substantial areas with rain rates higher than 30 mm/hr in the benchmark combined radar+radiometer retrievals are not matched by comparable estimates in the passive-MW-only retrievals. This subsection discusses these uncertainties and their order of magnitude.

Early (SSM/I era) passive MW precipitation approaches were based upon mostly statistical methods (Grody et al., 1991) that matched brightness temperature (TB) combinations to observed near-surface reference precipitation estimates made by rain gauges or by rain-gauge-trained ground radars. As such, these methods were tuned to the characteristics of the limited-domain input radar data used. The spatial and temporal variability in the precipitation microphysics and the nature of the weather conditions and surface conditions were not accounted for. The retrievals also failed to provide any physical estimate of the error in the precipitation rate. More recent passive MW Level-2 precipitation data products are more physically-based and account for the error inherent to the passive MW precipitation scheme itself. These include, but are not limited to, GPROF (Kummerow et al., 2015), surface emissivity-based methods (Turk et al., 2018), PRPS (Kidd et al., 2018b), k-nearest neighbor (Takbiri et al., 2019), TB “pseudo channel” schemes (Petty and Li, 2013), MIRS (Boukabara et al., 2011), the JAXA GSMaP scheme (Aonashi et al., 2009) and 1DVAR snowfall (Meng et al., 2017). Often, these methods apply data reduction to the input TB data to isolate the precipitation signal from the naturally-occurring variability in the input TB signal. Provided the collection of *a-priori* data used (in one way or another) is sufficiently representative of the conditions being sampled by the passive MW-based satellites, Bayesian-based methods provide a means to determine the error associated with the mean precipitation estimate.

In the merging algorithms that incorporate the Level-2 passive MW precipitation products and high-resolution, fast-refresh cycle geostationary satellite-based infrared (IR) observations, currently only one of these passive MW algorithms is used. For example, the IMERG Level-3 dataset relies upon passive MW precipitation produced by the GPROF algorithm (Kummerow et al., 2015), and the GSMaP product uses the JAXA passive MW algorithm (Aonashi et al., 2009). Therefore, only the error associated with this single passive MW precipitation technique affects the downstream Level-3 processing.

In reality, each of the passive MW precipitation methods makes different assumptions on many variable processes, such as the form of the particle size distribution, its spatial uniformity or inhomogeneity, etc. For GPM, the core satellite DPR-based precipitation algorithm has four main precipitation products, a DPR-only and a combined DPR+GMI algorithm (CORRA) (Greco et al., 2016), each with a Normal Scan (NS, or Ku-band only) and a Matched Scan (MS, or Ku+Ka-band) variant, for a total of four reported instantaneous estimates. Each of these retrieval algorithms make various simplifying assumptions to invert the measured radar reflectivity profiles into hydrometeor precipitation profiles. For example, the drop size distribution models used in the DPR algorithms are largely based on measurements from the tropics (Seto et al., 2013), which may not be applicable across the variety of weather systems encountered in the GPM coverage area. The drop size distribution models are selected based

on predefined precipitation types that are imperfectly identified from features in the radar reflectivity profiles. Another source of variability arises from the assumptions used to handle the variable surface radar surface cross section and (for CORRA) the surface emissivity variability (Munchak et al., 2016; Munchak et al., 2020). The multiple sources of uncertainty carry over into the passive MW-only precipitation profile estimates from each constellation MW radiometer.

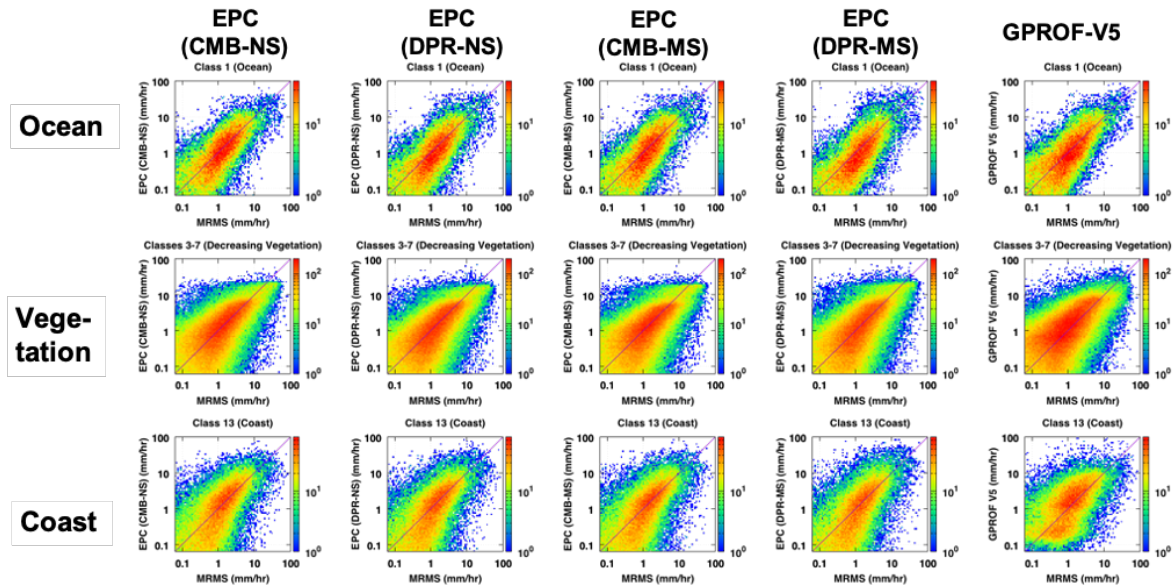


Figure 1.1.4. Comparison of five different instantaneous microwave retrievals versus the benchmark ground gauge-radar based Ground Validation Multi-Radar/Multi-Sensor estimates (horizontal axis; see section 1.2). From left, the EPC algorithm based on the GPM combined radar+radiometer algorithm (CORRA) Normal Scan (NS; Ku-band only) precipitation product, the EPC algorithm based on the GPM radar-only algorithm (DPR) Ku-band only precipitation product, the EPC algorithm based on the CORRA Matched Scan (MS; Ku+Ka-band) precipitation product, the EPC algorithm based on the GPM radar-only algorithm (DPR) Ku+Ka-band) precipitation product, and the Version 5 GPROF algorithm. The rows indicate data is from ocean, vegetated and coastal surface classes. Note the log-log scaling of each panel.

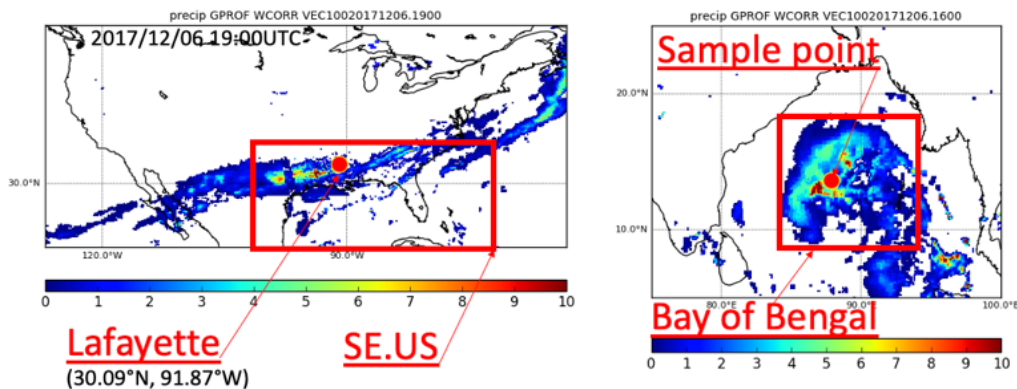


Figure 1.1.5. Maps showing the two locations of the case studies summarized in 1.1.3.2 and 1.1.3.3.

Currently, there is no consistent way to account for the range of uncertainty introduced in these instantaneous estimates, as they are used to make the passive MW constellation estimates,

and ultimately the Level-3 products including IMERG, GSMaP, CMORPH and others. However, one can estimate the magnitude of this uncertainty by comparing instantaneous retrievals to a common reference. Figure 1.1.4 shows a comparison of five different instantaneous GMI microwave retrievals (5 columns) relative to pixel-matched precipitation products derived from the benchmark U.S. ground radar-gauge Ground Validation Multi-Radar/Multi-Sensor (GV-MRMS) (Kirstetter et al., 2012, 2018b) products (horizontal axis; see Section 1.2), illustrating the uncertainty in any individual estimate to be above 100%. Since passive MW measurements are sensitive to the emission from the surface, the validation is separated by the underlying surface classification (ocean, vegetation, coastal), corresponding to each row. A common reference also makes it possible to diagnose and propagate the uncertainty to the Level-3 products (see Figure 1.1.12). Kidd et al. (2018a) used multi-radar multi-sensor (MRMS) to validate the GPROF algorithm across sensors.

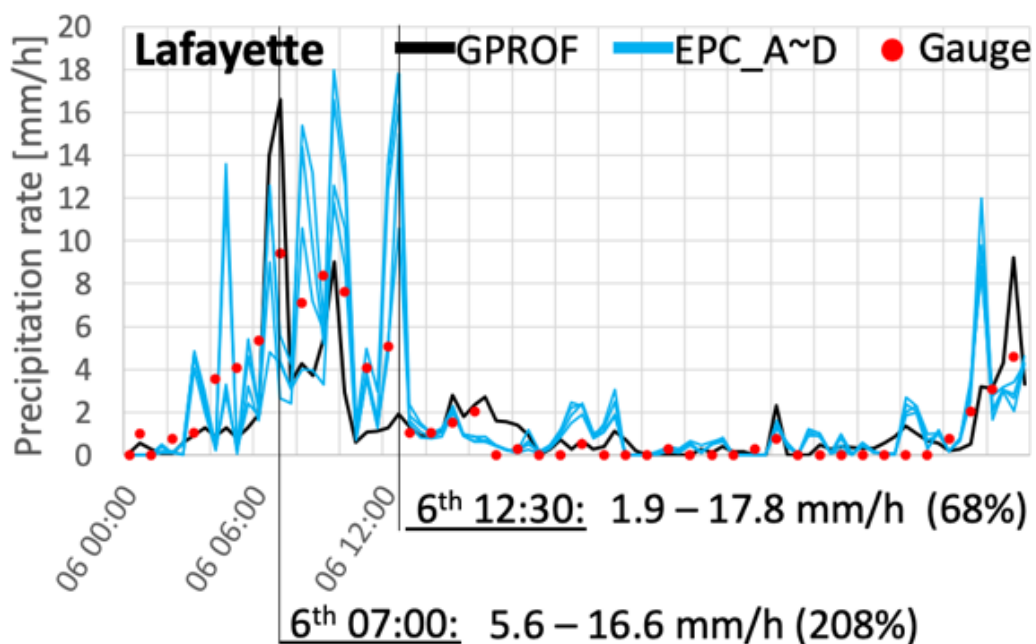


Figure 1.1.6. Time series of the five instantaneous passive microwave retrievals in Figure 1.1.4 for a specific 0.1-degree resolution element near Lafayette, LA (see Figure 1.1.4) on the ground, for a 42-hour period (0 UTC on 6 December 2017 through 18 UTC on December 7). The spread of the estimates is shown (up to 200% at times) as well as the discrepancy between the detection according to the satellite instrument and the lack of rain detected by the gauges at several times. This is most notable at 20 and 22 UTC on the 6th, at 12 and 13 UTC on the 7th.

While Figure 1.1.4 shows overall “bulk” comparisons of many individual per-pixel retrievals, the differences between each of the passive MW products at a specific pixel or “point” are more variable and can vary from location to location. To highlight an individual point location, Figure 1.1.6 shows the range of the five passive MW precipitation products from Figure 1.1.4 for a 42-hour period. The time series is from a specific 0.1-degree grid box point (the posted resolution of many Level-3 precipitation products) shown in Figure 1.1.5. In this example, the spread of the estimates is shown (up to 200% at times) as well as the discrepancy between the detection according to the satellite instrument and the lack of rain detected by the gauges at several times.

1.1.3.3. Errors introduced by revisit-gap mitigation

During the revisit gap between any two successive passive MW precipitation datasets, the precipitation is evolving. In Level-3 products such as CMORPH, GSMaP and IMERG, the precipitation evolution between successive passive MW precipitation datasets is accounted for by filtering/“morphing” methods. This process requires the use of ancillary data that is sampled frequently during the revisit gaps, to infer sufficient information to evolve the precipitation at one end of the temporal gap time-1 to the other time-2 (time-1 and time-2 being the observation times of the two passive MW satellites at the two ends of the revisit gap). This is done variously by tracking radiometrically cold IR cloud top patterns between successive 30-min imagery, or by tracking the motion of the precipitable water vapor patterns from global model reanalysis fields (Tan et al., 2019), or by tracking the motion of the IR-derived surface-precipitation fields, or using an empirically-derived filter based on these combined data. In effect, a several-degree box size is used to track the frequently-sampled data features from one time to the next, and to estimate the evolution of surface precipitation along these tracks.

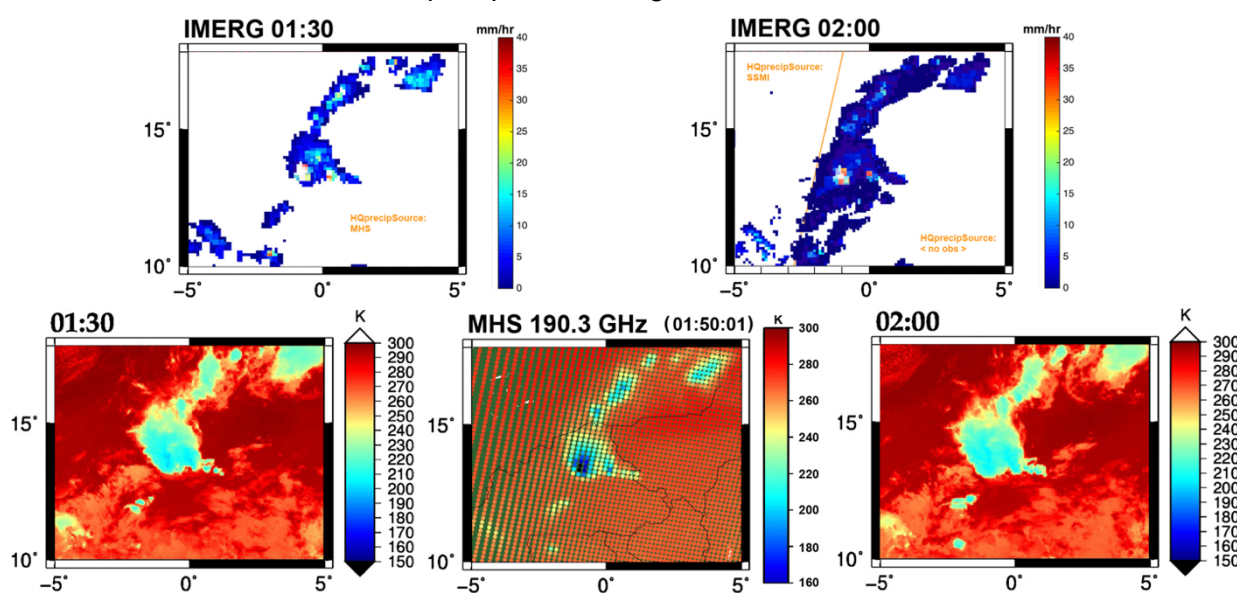


Figure 1.1.7. The top row shows the IMERG estimates of surface rain on 24 July 2014 at 0130 Z and 0200Z over a convective storm in West Africa, with marked differences between the rain fields at the two consecutive times despite the striking similarity of the geostationary IR observations at these times shown in the bottom row, along with the passive MW brightness temperatures measured by the MHS radiometer at 0150Z (Haddad et al., 2017).

Figure 1.1.7 illustrates the result in the case of a mesoscale convective system that developed over West Africa early on the morning of 24 July 2014. The surface rain estimated by the finest-resolution (30-min) IMERG product at 0130 Z is quite different from that at 0200 Z, in spite of the fact that the geostationary IR temperatures are quite similar at both times (lower panels). At 0130 UTC, the HQ precipitation source was from an MHS sounder. At 0200 UTC, the most-recent passive MW source was from the SSMIS (left side of the orange line) but only to the left of the orange line, with no passive MW data available in this 30-minute time on the right side of the line (where the storm was located). The main difference in the precipitation estimates is the large amount of low precipitation rates that appear at 0200 all around the storm as it was delineated at 0130, almost entirely due to the fact that between 0130 to 0200 there was a passive MW observation, by MHS at 0150Z, but between 0200 and 0230 the only MW observation was by SSMIS and missed this storm entirely, so that the estimates at 0200 are

strongly affected by revisit-gap mitigation. In this case, the precipitation at 0200 covers an area that is almost double that at 0130, the excess consisting entirely of rain rates below 2 mm/hr.

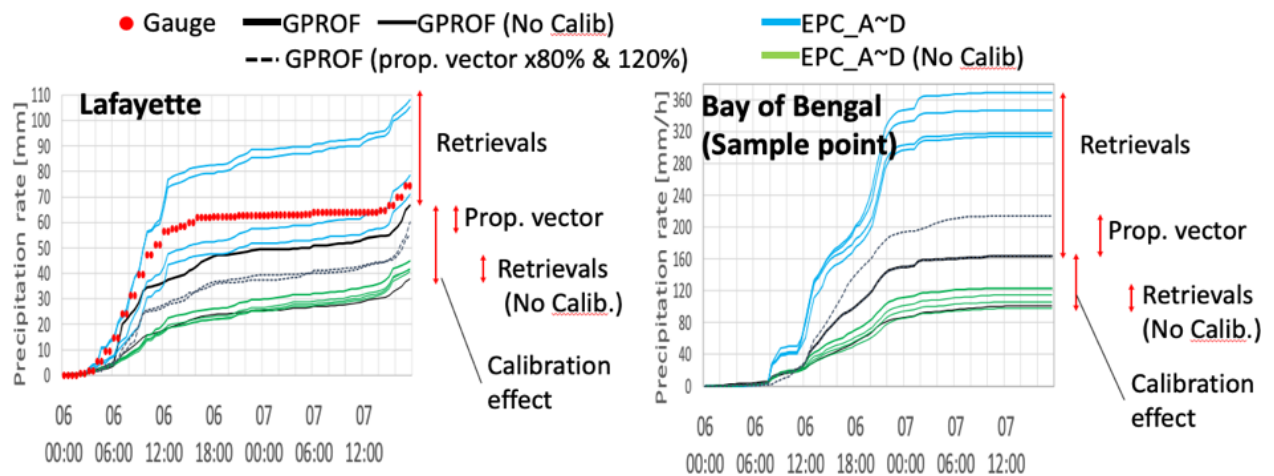


Figure 1.1.8. Accumulated precipitation for the same morphed products shown in Figure 1.1.6, for the Lafayette location (left) and the Bay of Bengal location (right). The comparison shows the result of using different passive MW precipitation products in the generation of the Level-3 merged satellite product, showing spreads that can grow to a factor of three at the end of the 42-hour period.

A more systematic evaluation of the cumulative effect of the interpolation was performed using IMERG as the evaluation medium. To that end, the IMERG technique was adapted into a “test mode” (IMERG-T) (Utsumi et al., 2018), where instead of feeding the IMERG process with the passive MW precipitation data from the GPROF algorithm, it can be fed with other, different passive MW precipitation retrievals. Figure 1.1.8 shows the same case as Figure 1.1.6, but in this example the accumulated precipitation is shown. The accumulated precipitation from the Bay of Bengal area in Figure 1.1.5 is also shown, as a side comparison. IMERG-T was run separately for each of the four passive MW algorithms in Figure 1.1.4. This was done with (blue lines) and without (green lines) the calibration step that is used in IMERG to assure that the histograms of the GPROF-GMI passive MW precipitation match the histograms of each of the other constellation sensors. The “spread” amongst the ten products (four EPC and GPROF, each with a calibrated and uncalibrated version) is shown by the red vertical line “Retrievals”. Figure 1.1.8 shows the net effect at a “pointwise” scale, which is the scale at which many Level-3 product users actually use and interpret these data for their analyses. While it shows only two locations, it does highlight the expected variability at the 0.1-degree scale. Other Level-3 product users may spatially average these native 0.1-degree, 30-minute data further, for example, into common 1-degree daily grid boxes (discussed in section 2 below) or 5-day pentads.

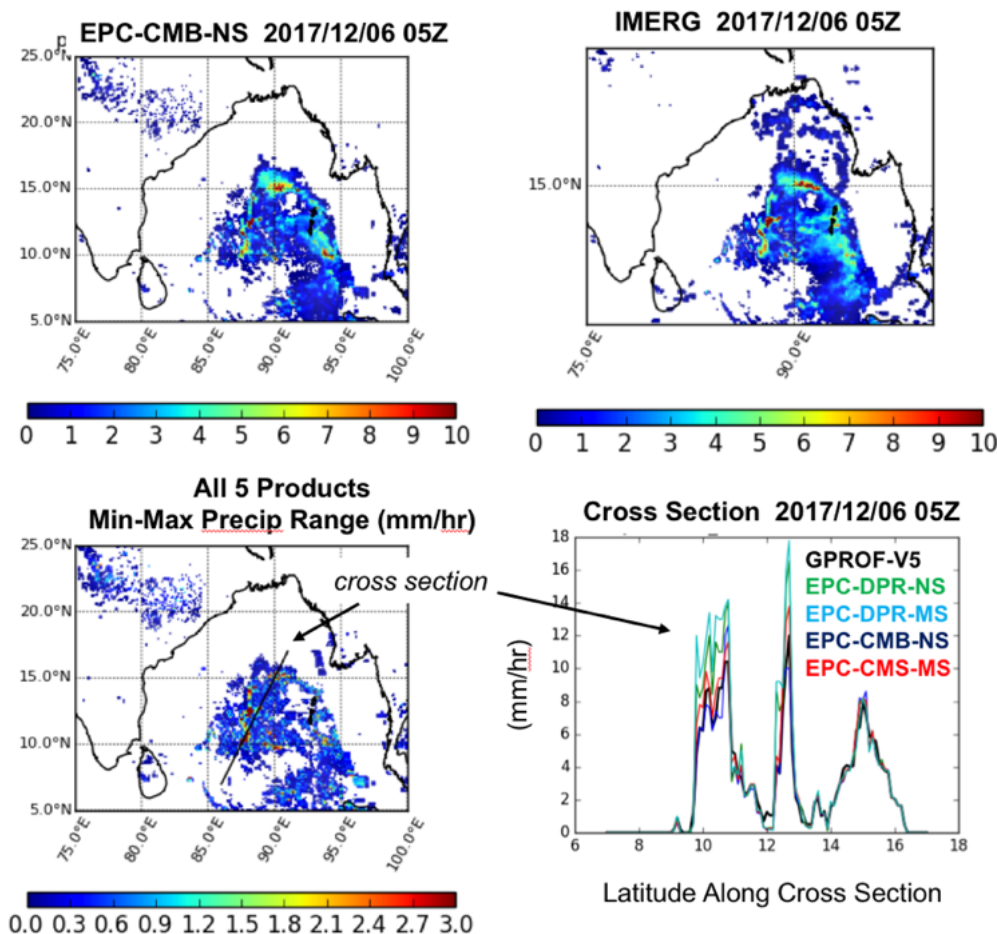


Figure 1.1.9. (Top right) Final IMERG precipitation product for the 30-minute interval ending at 05 UTC on 6 December 2017, showing an area in the Indian Ocean. **(Top left)** Corresponding image, except using the EPC CORRA-NS retrieval for each constellation radiometer (except MHS), to carry out the morphing procedure in IMERG-T. **(Lower left)** The ensemble spread (range of maximum-minus-minimum, in mm hr⁻¹) that results when each of the four EPC-based retrievals are fed through the IMERG-T morphing. **(Bottom right)** Final precipitation estimates along the cross-section line shown in the lower right panel for each of the four EPC-based retrievals. IMERG, which morphs using only GPROF precipitation, is shown in the black line.

In Figure 1.1.9, the official IMERG precipitation data valid at 0500 UTC on 6 December 2017 is shown in the upper right panel. This represents the average rain rate in the 30 minutes between 0430-0500 UTC. The collection of passive MW precipitation data products that feed into this IMERG estimate come from different satellite overpasses. Depending upon the orbit characteristics, some pixels in this area may have had a more recent “refresh” from a passive MW satellite than others. In this example, the passive MW precipitation products from the EPC products are based on the DPR+GMI combined Ku-band only product (Grecu et al., 2016). While the overall pattern of the precipitation is similar in the top two panels, there are small scale differences at the 0.1-degree level reported for the IMERG product.

This same process was repeated with the other three radar algorithms, each of whose passive MW precipitation data products were fed into the IMERG processing. The resultant ensemble spread expresses the overall range of variability in the final products considering that all of these factors are processed through IMERG. The lower left panel shows the range (maximum minus minimum) of values produced by the members of this ensemble.

To highlight the difference, the bottom right panel of Figure 1.1.9 shows the final precipitation estimates along the cross-section line shown in the lower right panel (IMERG, which morphs using only GPROF precipitation, is shown for comparison, in the black line), for each of the four EPC-based retrievals. The individual colors each represent the output when each of the four EPC-based estimates are used in the IMERG-T morphing procedure. Note the difference in some of the heaviest precipitation locations can be as much as 40% higher, but only slightly lower, than the IMERG product. *This ensemble analysis expresses the range of precipitation, considering each of the DPR-based precipitation estimates processed through each constellation radiometer, and processed through IMERG.*

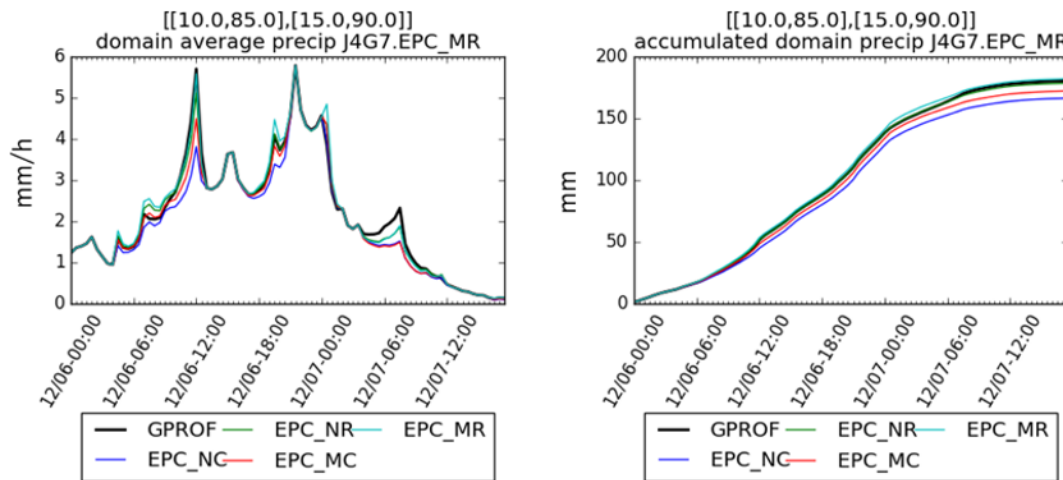


Figure 1.1.10. Analysis of the 36-hour period from 0 UTC on 6 December 2017 to 12 UTC on 7 December 2017, where the domain is a $5^\circ \times 5^\circ$ box in the Bay of Bengal. **(Left)** Domain-average IMERG precipitation product at each 30-minute time step. **(Right)** Accumulated precipitation. The domain-integrated accumulation at the end of the 36-hour period varies between 160 and 188 mm, a span of about 16% of the ensemble mean.

While Figure 1.1.9 highlights differences at the instantaneous (single overpass) scale, Figure 1.1.10 illustrates the cumulative effect of these same ambiguities when averaged over a $5^\circ \times 5^\circ$ domain and over the 36-hour duration of the storm. As expected, spatial and temporal averaging of the native fine-scale data reduces the instantaneous pointwise errors illustrated in Figure 1.1.9, but the uncertainty does not shrink to zero. Using a one-minute updating rain gauge network over Korea, Turk et al. (2009) examined the performance of the NRL-Blend fast-update precipitation product across telescoping space-time averaging scales. The space-time root mean square (RMS) error, mean bias, and correlation matrices were computed using various time windows for the gauge averaging, centered about the satellite observation time (this is necessary since the satellite measurement responds to the precipitation before it has fallen to the ground, where the gauges measure). For ± 10 minute rain gauge time windows (Figure 1.1.11), a correlation of 0.6 was achieved at 0.1-degree spatial scale by averaging over 3 days; coarsening the spatial scale to 1.8 degrees produced the same correlation by averaging over one hour. Finer than approximately 24-hours and 1-degree time and space scales, respectively, a rapid decay of the error statistics was obtained by trading off either spatial or time resolution.

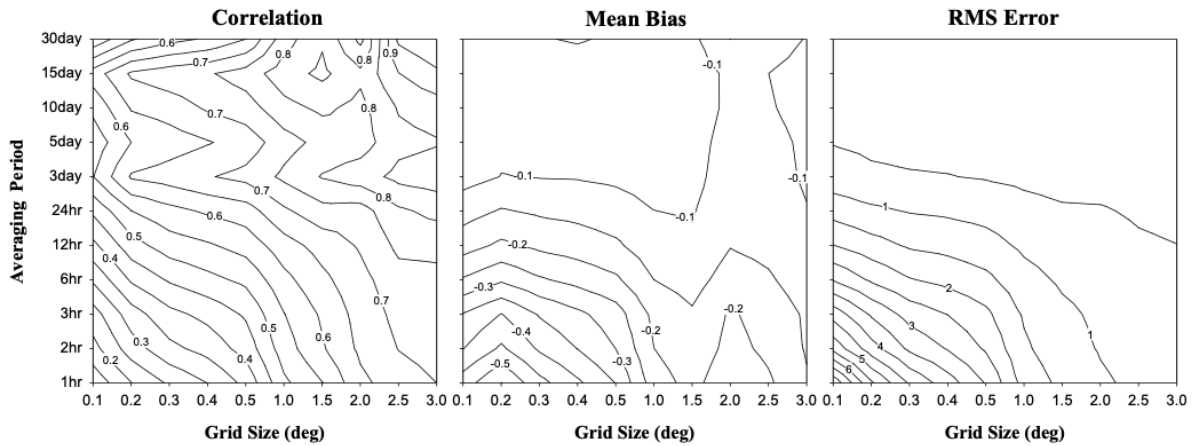


Figure 1.1.11. Space-time contour plots of the correlation coefficient, root mean square error and mean bias for the rain gauge network time window average of ± 10 minutes, centered about the time of the GMS satellite observation of Korea. The abscissa and ordinate of each contour plot denotes the spatial and temporal scales, respectively, used to average the rain gauge data and the NRL-blended satellite technique estimated rain (figure adapted from Turk et al., 2009).

1.1.3.4. Sensitivity to IR observations: Uncertainty in quantitative estimation and in interpolation during revisit gaps

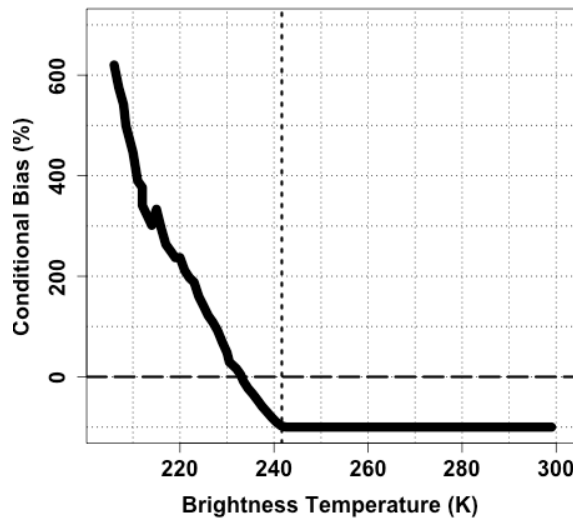


Figure 1.1.12. Relative bias in percentage between the PERSIANN-CCS precipitation estimates relative to the reference GV-MRMS as a function of the IR brightness temperature. This intrinsic bias results from the algorithm assumption that deeper clouds, represented by colder brightness temperatures, produce more surface rain. The conditional bias is a decreasing function of the brightness temperature following the redistribution assigning higher precipitation rates to colder brightness temperatures. The -100% bias above 242 K relates to missed precipitation that also results from the assumption (adapted from Kirstetter et al., 2018a).

Starting in the 1980s, when passive MW data was unavailable or scarce (routine SSMI data began in 1987), but geostationary IR measurements were routinely available hourly, the idea to use instantaneous IR radiances to estimate instantaneous surface rain was proposed and implemented. This was justified by the fact that, in convective storms, deeper clouds tend to produce more surface rain than shallower clouds (Arkin and Meissner, 1987; Huffman et al.,

1997). However, a cold IR temperature indicates a high cloud, which is not the same as a deep cloud. Even statistically, TRMM has established that the deepest clouds are not the ones that produce the highest surface rain rates (Hamada and Takayabu, 2016). The ambiguities are even greater away from the tropics, where the rain amounts produced by storms do not have a monotonic relation with the height of the cloud. IR radiances provide indirect information on the occurrence and magnitude of precipitation at the surface. Depending on the cloud type and life cycle, a given IR brightness temperature can be associated with various rain rates, since not all clouds produce precipitation or produce it at the same rate. IMERG combines IR-based Precipitation Estimation from Remotely Sensed Information using Artificial Neural Networks-Cloud Classification System (PERSIANN-CCS: Hong et al., 2004) and retrievals from passive MW estimates. As discussed earlier for passive MW estimates, the uncertainty associated with each PERSIANN-CCS retrieval is critically lacking for optimally merging PERSIANN-CCS outputs with passive MW precipitation and quantifying the propagation of this uncertainty into the final IMERG estimates. Kirstetter et al. (2018b) investigate this question with GV-MRMS over the U.S. over two summers of 2014–2015. They estimate that the PERSIANN-CCS intrinsic uncertainty, arising from assuming that deeper clouds produce more surface rain, can be described as a conditional bias typically ranging from –100% to +600% with the observed brightness temperatures (Fig. 4 in Kirstetter et al., 2018a, reproduced here in Figure 1.1.12). The volume of precipitation that is missed or erroneously detected is substantial (more than 50%), and the quantitative variability of correctly-detected precipitation is not well reproduced.

That is why the idea of using the frequently-available IR measurements to make instantaneous estimates of the underlying surface rain evolved to give rise to the less problematic concept of using them to guide the revisit-gap evolution estimation instead (Joyce et al., 2004, and references within). In this IR-based filtering, the features that are tracked represent cloud top patterns (IR cloud temperatures), rather than the actual evolution in time of the near-surface precipitation itself. The actual precipitation may be evolving faster or slower in space and intensity, in ways that are not easily approximated by locally linear tracking. For example, the precipitation at the surface may be moving slower or faster than the motion inferred from the upper cloud regions, or in extreme cases (where upper/lower vertical shear exists), moving in a different direction. To mitigate, certain algorithms such as CMORPH locally adjust the morphing tracking speed, based on comparisons with precipitation tracked from ground radars (Joyce and Xie, 2011). These discrepancies are a source of uncertainty in the Level-3 precipitation processing.

Using the IMERG-T analysis described above, Figure 1.1.13 illustrates the magnitude of the revisit-gap evolution speed uncertainty. The specific analysis quantifies the effect of artificially slowing down (or speeding up) the motion by 20, 30 or 50%. The difference in the final precipitation field is shown relative to the original precipitation. In this example, the largest differences are observed for the cases where the motion field was slowed down relative to what the IR-based tracking alone provides.

The “spread” at a given point due to the propagation vector variability was already illustrated in Figure 1.1.8 (highlighted by the vertical red arrow labeled “Prop. vector”) for each of the two 0.1-degree gridbox locations of Figure 1.1.5. In this example, the most noticeable effect occurs when the motion vectors were slowed down.

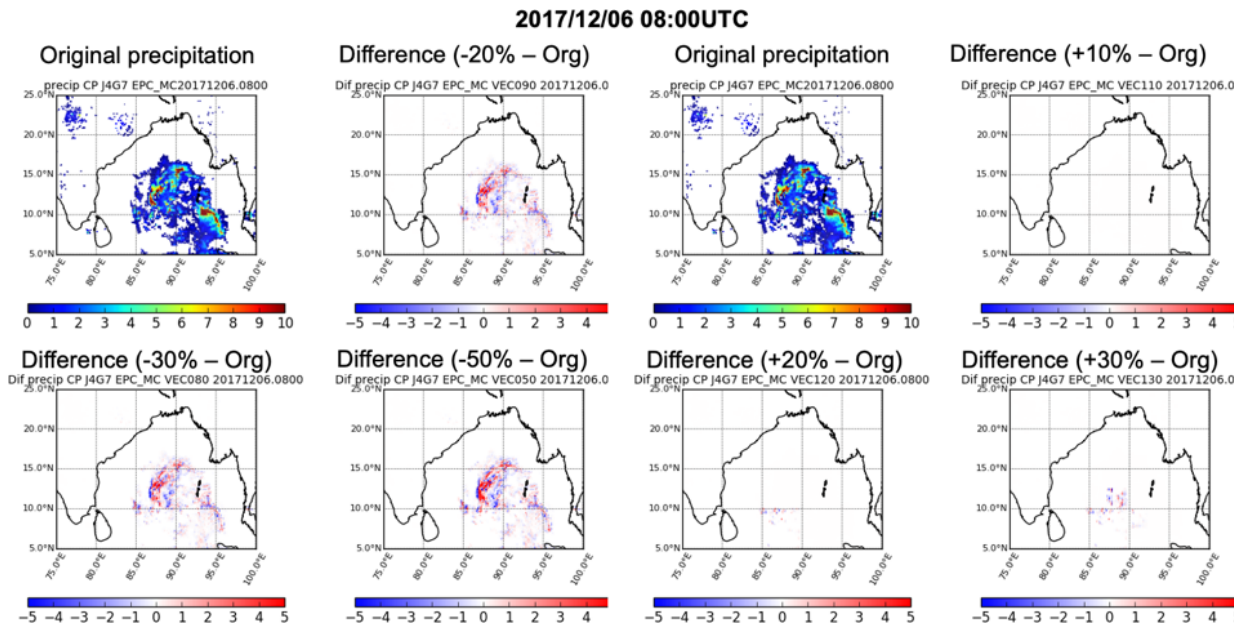


Figure 1.1.13. Left four panels: Net effect when the motion vector is slowed down by 20, 30 and 50% of its original value (upper left panel). **Right four panels:** Same, in the case when the motion vector is sped up by 20, 30 and 50% of its original value.

1.1.4. Summary of the assessment of intrinsic uncertainty

The Level-3 “sub-daily global merged satellite precipitation products” are typically reported on a fixed rectangular latitude-longitude grid at high spatial and temporal resolution (respectively 0.1° and ~ 0.5 hour). This subsection specifically concerned the uncertainties in these products at their reported resolution. These include the satellite precipitation products listed in Table 1.1.1, and are the building blocks for further coarser-resolution products included in later subsections.

The discussion above summarized the uncertainties that are inherent in the retrieval and processing steps that are used to produce the Level-3 estimates. These include the detection error, the passive MW and IR estimation errors, and the error incurred when using frequent IR information to fill long revisit gaps between passive MW estimates.

By themselves, passive MW observations alone are not capable of perfect detection. There is always an ambiguity between the passive MW TB and the particular atmospheric state that gives rise to these same TBs. For example, very light rainfall over ocean has a similar TB structure as a large amount of non-precipitating cloud water. For lack of a perfect benchmark reference, the exact sensitivity of a passive MW radiometer is challenging to determine.

The uncertainties in the passive MW estimates (second error above) originate from the limited sensitivity of the set of radiometer channels to the desired near-surface precipitation. As the signal that is measured by a passive MW or IR observation originates predominantly from the tops of the clouds, none of the instantaneous-level observations produced from these same sensors are directly and unambiguously sensitive to the underlying near-surface precipitation. Establishment of an absolute error is challenging since a common reference dataset is not globally available. Ground radars are an appropriate source of independent validation, but only cover specific continental land areas—and carry uncertainties of their own.

The majority of passive MW precipitation data is tied to specific local observing times by virtue of the operational nature of the host satellite platform. Only the GPM (and M-T) satellites currently orbit in a non-sun-synchronous orbit pattern capable of sampling (within its latitude coverage). This leads to lengthy gaps in satellite revisit, which are filled in with precipitation estimates created from geostationary-based IR observations. Currently this process is done via weighting of a priori prescribed uncertainties from the individual passive MW observations, with no regard for error in the speed or direction of the motion vectors used to transport the precipitation structure from one time period to the next. Few studies have been done in this regard, which warrant further study.

This section has quantified the order of magnitude of the uncertainty that *has to be expected* in today's merged satellite precipitation products at their native relatively-high (spatial and temporal) resolution, and which therefore exists as the current mutual ambiguity to be expected between the different Level-3 products. The following sections will describe, in more detail, independent validation of the uncertainty attributed to several of the precipitation datasets identified in this section, which includes the use of gauges and ground radars as an independent source.

Table 1.1.1. Global satellite precipitation products evaluated

<i>Product</i>	<i>Resolutions</i>	<i>Advantages</i>	<i>Disadvantages (in addition to possible local bias)</i>
Level-3 MiRS	When aggregated by user: no finer than single-instrument resolution (20–40 km) When pre-aggregated: daily	<ul style="list-style-type: none"> - Reasonably good sensitivity - Instantaneous estimate for every MW-constellation obs - Same approach over land or water 	Snapshots every ~80 minutes on average Revisit time could stretch to 3 hours
Level-3 GPROF	When aggregated by user: no finer than single-instrument resolution (20–40 km) When pre-aggregated: 0.5°/hourly (“3G68” product)	<ul style="list-style-type: none"> - Reasonably good sensitivity - Instantaneous estimate for every MW-constellation obs - Estimates calibrated by the reference GPM radiometer 	Snapshots every ~80 minutes on average Revisit time could stretch to 3 hours
Level-3 GPM radar/combined	When aggregated by user: 5 km When pre-aggregated: 0.25°/daily	<ul style="list-style-type: none"> - High direct sensitivity to surface rain - High spatial resolution (~5 km) 	Revisit time calculated in days

HOAPS	When aggregated by user: no finer than single-instrument resolution When pre-aggregated: 0.5°/6-hourly	Conically-scanning MW radiometers only	Ocean only
CMORPH	8 km/30 minutes (and various other pre-aggregated versions)	<ul style="list-style-type: none"> - Frequent temporal reporting (~30 mins) - Good spatial resolution (~25 km) - Uses MiRS for instantaneous MW estimates - Uses advection scheme from IR in between MW overpasses 	Persistence of any misdetection/amplification of estimation uncertainty
GSMaP	0.1°/hourly (and various other pre-aggregated versions)	<ul style="list-style-type: none"> - Frequent temporal reporting (~30 mins) - Good spatial resolution (0.1°) - Uses GSMaP_mwLUT for instantaneous MW estimates - Uses change in IR to adjust MW-estimated rain 	Persistence of any misdetection/amplification of estimation uncertainty
IMERG rt	0.1°/half-hourly	<ul style="list-style-type: none"> - Frequent temporal reporting (~30 mins) - Good spatial resolution - Uses GPROF for instantaneous MW estimates - Uses advection scheme from IR in between MW passes - Available within about 5 hours of obs 	Persistence of any misdetection/amplification of estimation uncertainty
IMERG late	0.1°/ half-hourly	<ul style="list-style-type: none"> - Frequent temporal reporting (~30 mins) - Good spatial resolution - Uses GPROF for instantaneous MW estimates - Available within a few weeks of obs 	Persistence of any misdetection/amplification of estimation uncertainty
IMERG science	0.1°/ half-hourly	<ul style="list-style-type: none"> - Frequent temporal reporting (~30 mins) - Good spatial resolution - Uses GPROF for instantaneous MW estimates 	Persistence of any misdetection/amplification of estimation uncertainty

		- Available 3 months after obs	
PERSIANN	0.04°/ half-hourly (PERSIANN-CCS)	- Long record back to ~ 1979 - NN approach accounts for regional variability	Mainly IR based – highly Indirect and non-monotone sensitivity to surface rain

Table 1.1.1. Listing of global satellite precipitation products with spatial resolution finer than 0.5 degrees and temporal resolution finer than 6-hourly, that have been evaluated by the IPWG validation subgroup

1.1.5. Recommendations

Recommendation 1.1.1: Encourage the a priori quantification of the uncertainty that should be expected in a given product, given the errors in the input and the uncertainties introduced by the product generation.

In the absence of an undisputed reference truth, the physical validation of an estimation method is very useful in putting bounds on the uncertainty that can be expected, given the author’s knowledge of the simplifying assumptions that were made to produce the estimates.

Recommendation 1.1.2: Encourage precipitation product providers to provide uncertainty estimates for each space/time scale of the final precipitation product.

Current global fine-resolution (< 0.1° horizontal, < daily temporal) satellite precipitation products are not mere aggregates of instantaneous satellite estimates. They rely on complex detection, estimation and filtering steps to produce a regularly-gridded product whose individual estimates carry quite a bit of uncertainty. These uncertainties vary from product to product, and consist of a mixture of misdetections and estimation errors that are compounded by revisit-gap-filling procedures that introduce additional uncertainty. Nevertheless, if these uncertainties are considered by the user, the passive MW-based products carry far less uncertainty than those based on geostationary IR alone or on rain gauges.

1.1.6. References

Aonashi, K., J. Awaka, M. Hirose, T. Kozu, T. Kubota, G. Liu, S. Shige, S. Kida, S. Seto and N. Takahashi, 2009: GSMaP passive microwave precipitation retrieval algorithm: Algorithm description and validation. *Journal of the Meteorological Society of Japan*, 87A, 119–136, <https://doi.org/10.2151/jmsj.87A.119>.

Arkin, P.A., and B.N. Meisner, 1987: The relationship between large-scale convective rainfall and cold cloud over the western hemisphere during 1982–84. *Monthly Weather Review*, 115, 51–74, [https://doi.org/10.1175/1520-0493\(1987\)115%3C0051:TRBLSC%3E2.0.CO;2](https://doi.org/10.1175/1520-0493(1987)115%3C0051:TRBLSC%3E2.0.CO;2).

Boukabara, S.A., K. Garrett, W. Chen, F. Iturbide-Sanchez, C. Grassotti, C. Kongoli, R. Chen, Q. Liu, B. Yan and F. Weng, 2011: MiRS: An All-Weather 1DVAR Satellite Data Assimilation and Retrieval System. *IEEE Transactions on Geoscience and Remote Sensing*, 49, 3249–3272, <https://doi.org/10.1109/TGRS.2011.2158438>.

Chen, H., B. Yong, J.J. Gourley, J. Liu, L. Ren, W. Wang, Y. Hong and J. Zhang, 2019: Impact of the crucial geographic and climatic factors on the input source errors of GPM-based global

satellite precipitation estimates. *Journal of Hydrology*, 575, 1–16, <https://doi.org/10.1016/j.jhydrol.2019.05.020>.

Ebert, E.E., J.E. Janowiak and C. Kidd, 2007: Comparison of near-real-time precipitation estimates from satellite observations and numerical models. *Bulletin of the American Meteorological Society*, 88, 47–64, <https://doi.org/10.1175/BAMS-88-1-47>.

Greco, M., W.S. Olson, S.J. Munchak, S. Ringerud, L. Liao, Z.S. Haddad, B.L. Kelley and S.F. Mclaughlin, 2016: The GPM combined algorithm. *Journal of Atmospheric and Oceanic Technology*, 33, 2225–2245, <https://doi.org/10.1175/JTECH-D-16-0019.1>.

Grody, N.C., 1991: Classification of snow cover and precipitation using the Special Sensor Microwave Imager. *Journal of Geophysical Research*, 96, 7423–7435, <https://doi.org/10.1029/91JD00045>.

Haddad, Z.S., R.C. Sawaya, S. Kacimi, O.O. Sy, F.J. Turk and J. Steward, 2017: Interpreting millimeter-wave radiances over tropical convective clouds. *Journal of Geophysical Research: Atmospheres*, 122, 1650–1664, <https://doi.org/10.1002/2016JD025923>.

Hamada, A., and Y.N. Takayabu, 2016: Improvements in Detection of Light Precipitation with the Global Precipitation Measurement Dual-Frequency Precipitation Radar (GPM DPR). *Journal of Atmospheric and Oceanic Technology*, 33, 653–667, <https://doi.org/10.1175/JTECH-D-15-0097.1>.

Hong, Y., K.-L. Hsu, S. Sorooshian and X. Gao, 2004: Precipitation Estimation from Remotely Sensed Imagery Using an Artificial Neural Network Cloud Classification System. *Journal of Applied Meteorology and Climatology*, 43, 1834–1853, <https://doi.org/10.1175/JAM2173.1>.

Hou, A.Y., R.K. Kakar, S. Neeck, A.A. Azarbarzin, C.D. Kummerow, M. Kojima, R. Oki, K. Nakamura and T. Iguchi, 2014: The Global Precipitation Measurement mission. *Bulletin of the American Meteorological Society*, 95, 701–722, <https://doi.org/10.1175/BAMS-D-13-00164.1>.

Hsu, K., X. Gao, S. Sorooshian and H.V. Gupta, 1997: Precipitation Estimation from Remotely Sensed Information Using Artificial Neural Networks. *Journal of Applied Meteorology and Climatology*, 36, 1176–1190, [https://doi.org/10.1175/1520-0450\(1997\)036<1176:PEFRSI>2.0.CO;2](https://doi.org/10.1175/1520-0450(1997)036<1176:PEFRSI>2.0.CO;2).

Huffman, G.J., R.F. Adler, P. Arkin, A. Chang, R. Ferraro, A. Gruber, J. Janowiak, A. McNab, B. Rudolf and U. Schneider, 1997: The Global Precipitation Climatology Project (GPCP) combined precipitation dataset. *Bulletin of the American Meteorological Society*, 78, 5–20, [https://doi.org/10.1175/1520-0477\(1997\)078%3C0005:TGPCPG%3E2.0.CO;2](https://doi.org/10.1175/1520-0477(1997)078%3C0005:TGPCPG%3E2.0.CO;2).

Huffman, G.J., D.T. Bolvin, D. Braithwaite, K. Hsu, R. Joyce, C. Kidd, E.J. Nelkin, S. Sorooshian, J. Tan and P. Xie, 2018: *IMERG Algorithm Theoretical Basis Document*, https://pmm.nasa.gov/sites/default/files/document_files/IMERG_ATBD_V5.2_0.pdf.

Joyce, R.J., J.E. Janowiak, P.A. Arkin and P. Xie, 2004: CMORPH: A Method that Produces Global Precipitation Estimates from Passive Microwave and Infrared Data at High Spatial and Temporal Resolution. *Journal of Hydrometeorology*, 5, 487–503, [https://doi.org/10.1175/1525-7541\(2004\)005<0487:CAMTPG>2.0.CO;2](https://doi.org/10.1175/1525-7541(2004)005<0487:CAMTPG>2.0.CO;2).

Joyce, R.J., and P. Xie, 2011: Kalman filter-based CMORPH. *Journal of Hydrometeorology*, 12, 1547–1563, <https://doi.org/10.1175/JHM-D-11-022.1>.

Kidd, C., J. Tan, P.-E. Kirstetter and W.A. Petersen, 2018a: Validation of the Version 05 Level 2 precipitation products from the GPM Core Observatory and constellation satellite sensors. *Quarterly Journal of the Royal Meteorological Society*, 144, 313–328, <https://doi.org/10.1002/qj.3175>.

Kidd, C., R. Roca and E. Stocker, 2018b: Development of the SAPHIR Precipitation Retrieval and Processing Scheme (PRPS). *Geophysical Research Abstracts*, Vol. 20, EGU2018-9356, EGU General Assembly 2018, <https://meetingorganizer.copernicus.org/EGU2018/EGU2018-9356.pdf>.

Kirstetter, P.-E., Y. Hong, J.J. Gourley, S. Chen, Z. Flamig, J. Zhang, M. Schwaller, W. Petersen and E. Amitai, 2012: Toward a Framework for Systematic Error Modeling of Spaceborne Precipitation Radar with NOAA/NSSL Ground Radar–Based National Mosaic QPE. *Journal of Hydrometeorology*, 13, 1285–1300, <https://doi.org/10.1175/JHM-D-11-0139.1>.

Kirstetter, P.-E., N. Karbalaee, K. Hsu and Y. Hong, 2018a: Probabilistic precipitation rate estimates with space-based infrared sensors. *Quarterly Journal of the Royal Meteorological Society*, 144 (Suppl. 1): 191–205, <https://doi.org/10.1002/qj.3243>.

Kirstetter, P.-E., W. Petersen and J.J. Gourley, 2018b: GPM Ground Validation Multi-Radar/Multi-Sensor (MRMS) Precipitation Reanalysis for Satellite Validation Product. Dataset available online from the NASA Global Hydrology Resource Center DAAC, Huntsville, Alabama, U.S.A. DOI: <http://dx.doi.org/10.5067/GPMGV/MRMS/DATA101>.

Kuligowski, R.J., Y. Li and Y. Zhang, 2013: Impact of TRMM Data on a Low-Latency, High-Resolution Precipitation Algorithm for Flash-Flood Forecasting. *Journal of Applied Meteorology and Climatology*, 52, 1379–1393, <https://doi.org/10.1175/JAMC-D-12-0107.1>.

Kummerow, C.D., J. Simpson, O. Thiele, W. Barnes, A.T.C. Chang, E. Stocker, R.F. Adler, A. Hou, R. Kakar, F. Wentz, P. Ashcroft, T. Kozu, Y. Hong, K. Okamoto, T. Iguchi, H. Kuroiwa, E. Im, Z. Haddad, G.J. Huffman, B. Ferrier, W.S. Olson, E.J. Zipser, E.A. Smith, T.T. Wilheit, G. North, T. Krishnamurti and K. Nakamura, 2000: The Status of the Tropical Rainfall Measuring Mission (TRMM) after Two Years in Orbit. *Journal of Applied Meteorology*, 39, 1965–1982, [https://doi.org/10.1175/1520-0450\(2001\)040<1965:TSOTTR>2.0.CO;2](https://doi.org/10.1175/1520-0450(2001)040<1965:TSOTTR>2.0.CO;2).

Kummerow, C.D., D.L. Randel, M. Kulie, N.Y. Wang, R. Ferraro, M.S. Joseph and V. Petkovic, 2015: The Evolution of the Goddard profiling algorithm to a fully parametric scheme. *Journal of Atmospheric and Oceanic Technology*, 32, 2265–2280, <https://doi.org/10.1175/JTECH-D-15-0039.1>.

Le Coz, C., and N. van de Giesen, 2020: Comparison of Rainfall Products over Sub-Saharan Africa. *Journal of Hydrometeorology*, 21, 553–596, <https://doi.org/10.1175/JHM-D-18-0256.1>.

Maggioni, V., M.R.P. Sapiano, R.F. Adler, Y. Tian and G.J. Huffman, 2014: An Error Model for Uncertainty Quantification in High-Time-Resolution Precipitation Products. *Journal of Hydrometeorology*, 15, 1274–1292, <https://doi.org/10.1175/JHM-D-13-0112.1>.

Maranan, M., A.H. Fink, P. Knippertz, L.K. Amekudzi, W.A. Atiah and M. Stengel, 2020: A Process-Based Validation of GPM IMERG and Its Sources Using a Mesoscale Rain Gauge Network in the West African Forest Zone. *Journal of Hydrometeorology*, 21, 729–749, <https://doi.org/10.1175/JHM-D-19-0257.1>.

Meng, H., J. Dong, R. Ferraro, B. Yan, L. Zhao, C. Kongoli, N.-Y. Wang and B. Zavadsky, 2017: A 1DVAR-based snowfall rate retrieval algorithm for passive microwave radiometers. *Journal of Geophysical Research: Atmospheres*, 122, 6520–6540, <https://doi.org/10.1002/2016JD026325>.

Munchak, S.J., S. Ringerud, L. Brucker, Y. You, I. de Gelis and C. Prigent, 2020: An Active–Passive Microwave Land Surface Database From GPM. *IEEE Transactions on Geoscience and Remote Sensing*, 58, 6224–6242, <https://doi.org/10.1109/TGRS.2020.2975477>.

Munchak, S.J., R. Meneghini, M. Grecu and W.S. Olson, 2016: A consistent treatment of microwave emissivity and radar backscatter for retrieval of precipitation over water surfaces. *Journal of Atmospheric and Oceanic Technology*, 33, 215–229, <https://doi.org/10.1175/JTECH-D-15-0069.1>.

Negri, A.J., T.L. Bell and L. Xu, 2002: Sampling of the diurnal cycle of precipitation using TRMM. *Journal of Atmospheric and Oceanic Technology*, 19, 1333–1344, [https://doi.org/10.1175/1520-0426\(2002\)019%3C1333:SOTDCO%3E2.0.CO;2](https://doi.org/10.1175/1520-0426(2002)019%3C1333:SOTDCO%3E2.0.CO;2).

Petty, G.W., and K. Li, 2013: Improved passive microwave retrievals of rain rate over land and ocean. Part I: Algorithm description. *Journal of Atmospheric and Oceanic Technology*, 30, 2493–2508, <https://doi.org/10.1175/JTECH-D-12-00144.1>.

Roca, R., H. Brogniez, P. Chambon, O. Chomette, S. Cloché, M.E. Gosset, J.-F. Mahfouf, P. Raberanto and N. Viltard, 2015: The Megha-Tropiques mission: A review after three years in orbit. *Frontiers in Earth Science* 3, 17, <https://doi.org/10.3389/feart.2015.00017>.

Seto, S., T. Iguchi and T. Oki, 2013: The Basic Performance of a Precipitation Retrieval Algorithm for the Global Precipitation Measurement Mission’s Single/Dual-Frequency Radar Measurements. *IEEE Transactions on Geoscience and Remote Sensing*, 51, 5239–5251, <https://doi.org/10.1109/TGRS.2012.2231686>.

Sun, Q., C. Miao, Q. Duan, H. Ashouri, S. Sorooshian and K.-L. Hsu, 2018: A review of global precipitation datasets: data sources, estimation, and intercomparisons. *Reviews of Geophysics*, 56, 1–29, <https://doi.org/10.1002/2017RG000574>.

Takbiri, Z., A. Ebtehaj, E. Foufoula-Georgiou, P.-E. Kirstetter and F.J. Turk, 2019: A Prognostic Nested k-Nearest Approach for Microwave Precipitation Phase Detection over Snow Cover. *Journal of Hydrometeorology*, 20, 251–274, <https://doi.org/10.1175/JHM-D-18-0021.1>.

Tan, J., W.A. Petersen and A. Tokay, 2016: A Novel Approach to Identify Sources of Errors in IMERG for GPM Ground Validation. *Journal of Hydrometeorology*, 17, 2477–2491, <https://doi.org/10.1175/JHM-D-16-0079.1>.

Tan, J., G.J. Huffman, D.T. Bolvin and E.J. Nelkin, 2019: IMERG V06: Changes to the Morphing Algorithm. *Journal of Atmospheric and Oceanic Technology*, 36, 2471–2482, <https://doi.org/10.1175/JTECH-D-19-0114.1>.

Turk, F.J., P. Arkin, M.R.P. Sapiiano and E.E. Ebert, 2008: Evaluating high-resolution precipitation products. *Bulletin of the American Meteorological Society*, 89, 1911–1916, <https://doi.org/10.1175/2008BAMS2652.1>.

Turk, F.J., B.-J. Sohn, H.-J. Oh, E.E. Ebert, V. Levizzani and E.A. Smith, 2009: Validating a rapid-update satellite precipitation analysis across telescoping space and time scales. *Meteorology and Atmospheric Physics*, 105, 99–108, <https://doi.org/10.1007/s00703-009-0037-4>.

Turk, F.J., Z.S. Haddad, P. Kirstetter, Y. You and S. Ringerud, 2018: An observationally based method for stratifying *a priori* passive microwave observations in a Bayesian-based precipitation retrieval framework. *Quarterly Journal of the Royal Meteorological Society*, 144, Issue S1, 145–164, <https://doi.org/10.1002/qj.3203>.

Ushio, T., K. Sasashige, T. Kubota, S. Shige, K. Okamoto, K. Aonashi, T. Inoue, N. Takahashi, T. Iguchi and M. Kachi, 2009: A Kalman Filter Approach to the Global Satellite Mapping of Precipitation (GSMaP) from Combined Passive Microwave and Infrared Radiometric Data. *Journal of the Meteorological Society of Japan*, 87A, 137–151, <https://doi.org/10.2151/jmsj.87A.137>.

Utsumi, N., F.J. Turk, Z. Haddad, G. Huffman and D. Bolvin, 2018: *A Self-Consistent Ensemble Approach to Propagate Estimation, Calibration, and Evolution Uncertainties through Global Precipitation Measurement Surface Precipitation Mapping*. Proceedings from a NASA Precipitation Measurements Mission science team meeting held in Phoenix, Arizona, U.S.A., from 8–11 October 2018, <https://gpm.nasa.gov/research/meetings/2018-pmm-science-team-meeting>.

Utsumi, N., F.J. Turk, Z.S. Haddad, P.-E. Kirstetter and H. Kim, 2020: Evaluation of precipitation vertical profiles estimated by GPM-era satellite-based passive microwave retrievals. *Journal of Hydrometeorology*, <https://doi.org/10.1175/JHM-D-20-0160.1>.

You, Y., V. Petkovic, J. Tan, R. Kroodsma, W. Berg, C. Kidd and C. Peters-Lidard, 2020: Evaluation of V05 Precipitation Estimates from GPM Constellation Radiometers Using KuPR as the Reference. *Journal of Hydrometeorology*, 21, 705–728, <https://doi.org/10.1175/JHM-D-19-0144.1>.